Martin Straka*, Christian Koglin, and Thomas Eichler

# Segmental orifice plates and the emulation of the 90°-bend

## Segmentblenden und die Nachbildung des 90°- Krümmers

**Abstract:** The 90°- bend represents the most common structural element in piping systems and can have a significant impact on the measuring accuracy of flow meters installed downstream. Within the type-approval procedure of water meters, its impact is emulated by means of a segmental orifice plate with a segment area of 7 % (SOP7). In research and development, coverage rates of 33 % (SOP33) or more are sometimes used as an alternative. The purpose of this study is to evaluate the comparability of the flow conditions and their influence on the measurement deviation of flow meters, which is the basic requirement for using SOPs as a substitute for the 90°- bend. We present laser Doppler measurements downstream of an SOP33 and a 90°- bend and describe the flow development in a distance range from 2 to 30 diameters. Besides a quantitative comparison with performance indicators, the measurements are used to model the response of an ultrasonic and electromagnetic flow meter, including recent investigations of an SOP7. The results demonstrate the consistently poor agreement between the SOP7 and the 90°- bend, whereas the SOP33 provides similar flow conditions starting at a distance of 10 diameters. Further studies are necessary to develop a disturbance generator emulating the near-field range.

**Keywords:** Flow measurement, standardization, disturbed flow conditions, LDA.

**Zusammenfassung:** Der 90°- Krümmer ist das am häufigsten vorkommende Bauteil in Rohrleitungen und kann die Messgenauigkeit von stromab installierten Durchflusssensoren signifikant beeinträchtigen. Im Rahmen der Bauartzulassungsprüfung von Wasserzählern wird sein Einfluss mit Hilfe einer Segmentblende nachgebildet, die 7 % des Querschnitts abdeckt (SOP7). In der Forschung kom-

men auch größere Abdeckungsgrade wie 33 % zum Einsatz (SOP33). Ziel dieser Studie ist es, die bei der Verwendung der Blenden vorausgesetzte Vergleichbarkeit mit den Strömungsbedingungen des 90°- Krümmers und deren Einfluss auf die Messabweichung von Durchflusssensoren zu evaluieren. Wir zeigen Laser-Doppler-Messungen stromab einer SOP33 und eines 90°- Krümmers und beschreiben die Strömungsentwicklung im Abstand von 2 bis 30 Durchmessern. Unter Einbeziehung der Messdaten einer SOP7 wird ein quantitativer Vergleich mittels Kennzahlen durchgeführt und der Einfluss der Strömung auf einen Ultraschall- und elektromagnetischen Durchflusssensor modelliert. Die Ergebnisse zeigen eine durchgängig schlechte Übereinstimmung zwischen der SOP7 und dem 90°- Krümmer, während die SOP33 ab einem Abstand von 10 Durchmessern ähnliche Strömungsbedingungen erzeugt. Die Darstellung des Nahfelds erfordert die Entwicklung eines neuen Störkörpers.

**Schlagwörter:** Durchflussmessung, Normung, gestörte Strömungsbedingungen, LDA.

# 1 Introduction

In flow measurement applications, installation components such as bends, valves and pumps create flow disturbances deviating from the swirl-free and symmetric reference state. The most commonly used part in domestic and industrial piping systems is the 90°- bend (see Fig. 1 a). Non-ideal flow conditions can have a significant impact on the measuring accuracy of flow meters installed downstream. The development of meter designs and standardized type-approval procedures are therefore accompanied by tests including the most relevant flow disturbances.

At test facilities, the construction of a reproducible measurement section with bends is not always possible, especially for larger pipe diameters. For this reason, the investigated flow conditions are emulated by means of designated disturbance generators. In legal metrology, tests are limited to a small selection of disturbed flow categories.

*Corresponding author: Martin Straka, Physikalisch-Technische Bundesanstalt, Abbestr. 2–12, 10587 Berlin, Germany, e-mail: martin.straka@ptb.de, ORCID:
https://orcid.org/0000-0002-4175-9238
**Christian Koglin, Thomas Eichler,** Physikalisch-Technische Bundesanstalt, Abbestr. 2–12, 10587 Berlin, Germany
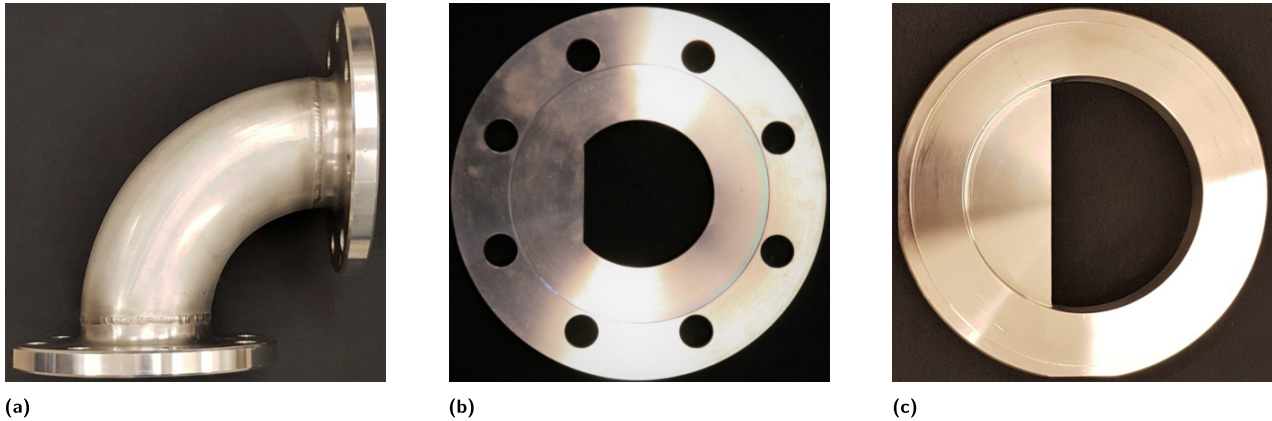
(a)          (b)          (c)

**Figure 1:** Geometrical specifications of the test objects. (a): 90°- bend according to the standards for butt-welding pipe fittings [6, 7] in DN 100 (inner diameter $D = 100.0$ mm) with a bending radius of $1.425 \cdot D$; (b): Segmental orifice plate (SOP) according to the standards for water meters [4, 3] in DN 80 ($D = 80.0$ mm) with a segment area of $A \approx 7\%$ (segment height $s = 12.5\% \cdot D$); (c): SOP in DN 100 ($D = 100.0$ mm) with $A \approx 33\%$ ($s = 36.75\% \cdot D$).

In addition to a pair of swirl generators representing the single-vortex structures created by double bend configurations, the standards for water meters [4, 3] include a segmental orifice plate (SOP) that aims at creating "an asymmetric velocity profile usually found downstream of a protruding pipe joint, single [ 90°-] bend or a gate valve not fully opened". Due to its frequent appearance, the 90°- bend constitutes the most important element in the aspired emulation range. As depicted in Fig. 1 (b), the circular segment area of the standardized SOP covers ≈ 7 % of the pipe's cross section (SOP7).

Outside the context of standardized testing, the variety of disturbance generators is much larger. In research and development, SOPs with a covered area of ≈ 33 % (SOP33, see Fig. 1 c) or higher are sometimes used as an alternative to improve the performance of meters exposed to the 90°- bend.

90°- bends have been investigated for over a hundred years and the internal flow phenomena are well understood. A historical review is given by Kalpakli [15]. Recent experimental and numerical studies regarding vortex structures, pressure losses, flow separation and swirl switching include [12, 24, 9, 26], whereas studies investigating the impact on flow meters include [27, 16]. The standards for butt-welding pipe fittings [6, 7] distinguish between bending radii of around 1.0, 1.5 and 2.5 pipe diameters, 1.5 being the most common in piping systems smaller than DN 400. Inside the bend, the fast-moving core flow experiences a stronger centrifugal force and shifts towards the outer radius, while the slowly moving fluid is forced to escape along the wall and returns towards the pipe center from the side of the inner curvature. This re-

sults in a highly asymmetric velocity profile downstream, superimposed by a pair of counter-rotating non-axial velocity structures, referred to as Dean vortices [10] (see Fig. 7).

The flow development downstream of an SOP7 was investigated by Eichler [13], who described a displacement of the core flow to the opposite side of the pipe at a distance of one diameter. Further downstream, the velocity peak was found located on the orifice side. An SOP33 was studied by Straka et al. [23]. A much stronger asymmetry and again, the shift of the peak velocity region as a result of the Dean vortices were observed. In contrast to the 90°- bend, where the rotating movement guides the low velocity region towards the pipe center, the Dean vortices downstream of the SOPs were found to initially guide the accelerated core flow towards the pipe center.

In view of these differences, the emulation of the 90°- bend cannot be a generally valid one-to-one mapping independent of the downstream distance or the geometrical parameters of the SOP, despite the mutual presence of asymmetry and Dean vortices. Given the potential consequences for the efficiency of legal metrology controls and the development of reliable flow meters, the purpose of this study is to evaluate the comparability of the flow conditions and their influence on the measurement deviations of flow meters, which is the basic requirement for using SOPs as a substitute for 90°- bends.

We present laser Doppler anemometry (LDA) measurements downstream of an SOP33 and a 90°- bend and demonstrate the qualitative differences of the near- and far-field flow development through a description of the flow patterns. Furthermore, we carry out a quantitative

comparison by means of performance indicators, including the measurements of an SOP7 investigated by Eichler [13].

An analysis with performance indicators is a mathematical tool to describe the individual features of a (disturbed) velocity profile. It can be used to quantify the degree of similarity between different flow conditions, in which a transferability to the measuring error of flow meters is implied through the comparability of the effect caused by the extent of a certain flow feature.

In addition, the LDA measurements are used to model the response of an ultrasonic (UFM) and electromagnetic flow meter (EFM) and describe the meter errors resulting from the different flow conditions. UFMs and EFMs are often found in industrial piping systems and are increasingly used in domestic applications.

Both the flow analysis and the performance of the modeled flow meters exposed to the flow conditions created by the orifices and the 90°- bend allow for an evaluation of the disturbance generators with regard to the quality of the emulation.

## 2 Methods

### 2.1 Experimental setup

LDA measurements of the axial and horizontal velocity components $w$ and $u$ were taken downstream of the SOP33 and the 90°- bend at distances of approximately 2, 5, 10, 15, 20 and 31 pipe diameters ($D$). The flow test facility including the measurement sections built in the nominal diameter DN 100 ($D$ = 100.0 mm) is illustrated in Fig. 2. The geometrical specifications of the test objects in DN 100 as

well as the SOP7 investigated by Eichler [13] in DN 80 are depicted in Fig. 1, whereas the LDA setup is illustrated in Fig. 3.
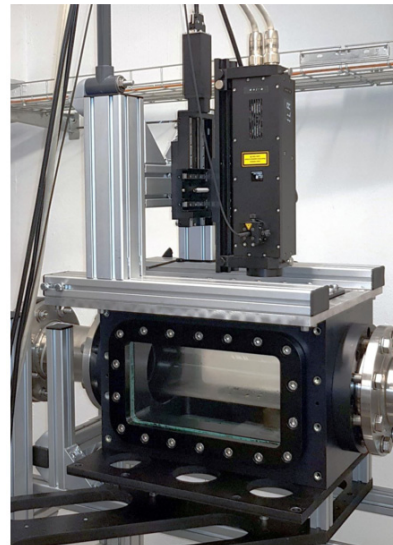


**Figure 3:** LDA setup consisting of the 2D laser probe (*ILA GmbH* fp50-shift with wavelengths of 532 and 561 nm), its traversing system and the optical access. Prior to the measurement campaign, the probe was calibrated on a velocity standard [25] at the National Metrology Institute of Germany (PTB).

Special care was taken with regard to the alignment of the LDA probe and the installation of the measurement setup. The flow conditioners, pipes, the SOP33, the 90°- bend and the optical access are connected by centering rings using a sliding fit with a tolerance of 40 μm. All components including the glass pipe have a wall roughness ≤ 5 μm and the same inner diameter of 100.0 mm with a tolerance of ±50 μm. At the end of the inlet section, fully
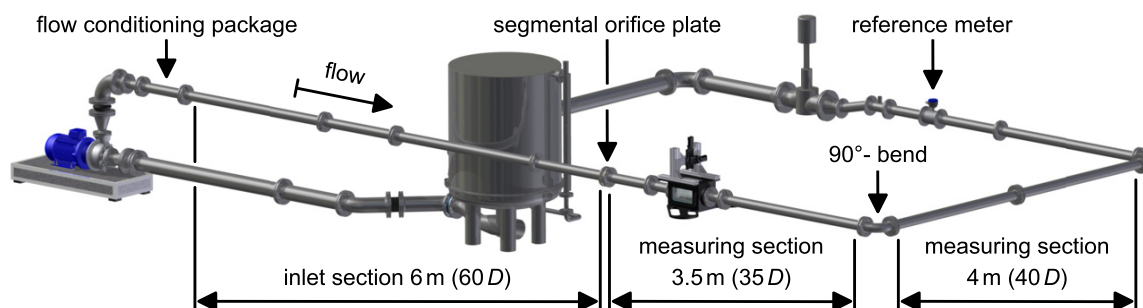


**Figure 2:** Long-term ultrasonic and laser measurement facility (LULA) at the National Metrology Institute of Germany (PTB). LULA provides an inlet section of 6 m preceded by a flow conditioning package including a tube bundle straightener and a Zanker plate as defined in ISO 5167 [2]. There are two measurement sections for the investigation of the segmental orifice plate and the 90°- bend with a length of 3.5 and 4 m, respectively. A *KROHNE* Optiflux 5300 with an expanded uncertainty of $U$ = 0.2 % ($k$ = 2) [20] is used as a reference meter.
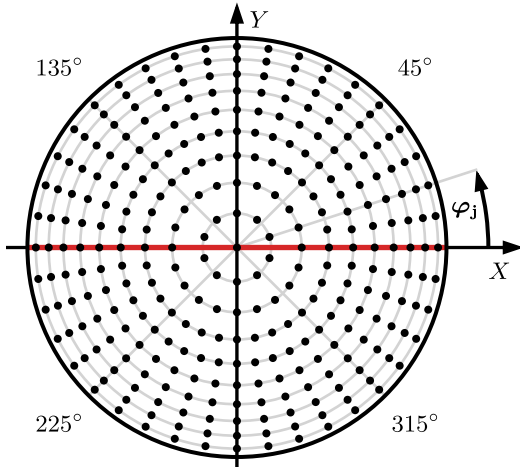
**Figure 4:** LDA measurement grid as described by Straka et al. [22] with $N_\varphi = 20$ radial paths ($\Delta\varphi = 9°$) and a total of 303 points. The red line indicates the position of the horizontal grid path with $y = 0$ ($\varphi_1 = 0°$), used for the definition of the maximum horizontal velocity $u_{max}$.

developed reference conditions were verified by means of LDA measurements. On every location in the LDA grid depicted in Fig. 4, a minimum number of 25 000 velocity values was determined. Within each time frame, the averaged values were normalized with the mean flow rate of the reference meter according to the procedure described in VDI/VDE 2640 [1].

Measurements were performed at a water temperature of 30 °C (kinematic viscosity $\nu = 0.8 \times 10^{-6}\,\mathrm{m^2\,s^{-1}}$) and volumetric velocities $w_{vol}$ of 0.4 and 4.0 m s$^{-1}$. This corresponds to flow rates of 11.32 and 113.20 m$^3$ h$^{-1}$ and Reynolds numbers $Re = w_{vol} \cdot D/\nu$ of $5 \times 10^4$ and $5 \times 10^5$.

## 2.2 Quantification by means of performance indicators

In the quantitative analysis, we used modified versions of the profile, asymmetry and turbulence factor ($K_P$, $K_A$, $K_{Tu}$) from a set arranged by Müller [19] to evaluate the flow conditions at test rigs in the framework of disturbance tests according to the standards for heat meters [5]. In combination, they describe the shape, asymmetry and turbulence and cover all major flow features of the axial velocity component. As suggested by Straka et al. [22], mean and maximum values are used to obtain a representation for the entire profile. In addition, we introduce the maximum horizontal velocity $u_{max}$ as an estimate for the swirling intensity of the Dean vortices.

### 2.2.1 Definition of the mean profile factor

The mean profile factor $\langle K_P \rangle$ is given by

$$\langle K_P \rangle = \frac{1}{N_\varphi} \sum_{i=1}^{N_\varphi} \frac{\int_{-R}^{R}(w_m - w)\,\mathrm{d}r}{\int_{-R}^{R}(w_{s.m} - w_s)\,\mathrm{d}r} \tag{1}$$

and constitutes the arithmetic mean of the individual values of $K_P$ for the $N_\varphi = 20$ radial paths of the LDA measurement grid (see Fig. 4). For a wide range of disturbed flow conditions, it describes the profile shape of a velocity distribution, that can be either pointed ($\langle K_P \rangle > 1$), flattened or concave ($\langle K_P \rangle < 1$) or equal to a fully developed reference ($\langle K_P \rangle = 1$). (Due to the definition with the velocity in the pipe center, these correlations are not necessarily applicable at the presence of a strong asymmetry.)

In the equation, $w$ and $w_s$ denote the local velocities of the measurement data and the reference profile in the axial direction, whereas $w_m$ and $w_{s.m}$ designate the respective values in the pipe center. As a reference, the analytical profile described by Gersten and Herwig [14] with updated constants given in Merzkirch [17] was used. The terms in the numerator and denominator placed in brackets are integrated over the radial position $r$ in the closed interval of $r = [-R, R]$, where $R$ denotes the pipe radius. Both integrals can be solved analytically after replacing the LDA data points with piecewise sub-splines as described by Akima [8]. Moreover, the wall function defined by Straka et al. [22] is used to interpolate the velocity distribution between the outermost measurement points and the wall. (The representation with sub-splines and the wall function are also used below for the calculation of $K_A$, $Q_{UFM}$ and $Q_{EFM}$.) A comprehensible derivation of $K_P$ including a graphical representation is given in Müller [19].

### 2.2.2 Definition of the mean asymmetry factor

The mean asymmetry factor $\langle K_A \rangle$ is given by

$$\langle K_A \rangle = \frac{1}{N_\varphi} \sum_{i=1}^{N_\varphi} \left| \frac{\int_{-R}^{R} r \cdot w\,\mathrm{d}r}{\int_{-R}^{R} w\,\mathrm{d}r} \cdot \frac{1}{D} \right| \cdot 100\,[\%] \tag{2}$$

and corresponds to the arithmetic mean of the absolute values of $K_A$ in the grid paths. It describes the radial displacement of the profile's velocity centroid expressed in percent and is therefore a measure for the degree of asymmetry. In the equation, the first term within the vertical bars is equivalent to the mathematical definition of a geometrical centroid. A division by the pipe diameter $D$ yields a relative difference with respect to the path length.

### 2.2.3 Definition of the maximum turbulence factor

The maximum turbulence factor $K_{Tu.\,max}$ is given by

$$K_{Tu.\,max} = \frac{\max\,(Tu)}{Tu_s}\ , r \leq 0.2 \cdot R \tag{3}$$

and corresponds to the maximum value of $K_{Tu}$. It describes the ratio between the highest degree of turbulence $Tu$ within a specified core region of the pipe ($r \leq 0.2 \cdot R$) and the theoretical degree of turbulence $Tu_s$ in the center, using an approximation described by Durst et al. [11]. $Tu$ is the coefficient of variation for the velocity samples at each grid point calculated as the ratio between the standard deviation to the mean.

### 2.2.4 Definition of the maximum horizontal velocity

In contrast to the performance indicators representing the axial component, the maximum horizontal velocity $u_{max}$ defined as

$$u_{max} := \frac{\max\,(|u|)}{w_{vol}}\ , y = 0 \tag{4}$$

is based on the horizontal velocity component $u$ in the direction of $x$. It describes the absolute maximum of $u$ on the horizontal grid path, where $y = 0$ and $\varphi = 0°$ (highlighted red in Fig. 4), normalized with the volumetric velocity $w_{vol}$. Although a complete visualization of the two-vortex Dean structure as illustrated in Fig. 7 (i) requires the measurement of both secondary components $u$ and $v$, $u_{max}$ allows for a good approximation of the swirling velocity.

## 2.3 Modeling of flow meters

In what follows, the mathematical models used to simulate the response of an ultrasonic and electromagnetic flow meter are described. In contrast to mechanical meter designs, the basic form of UFMs and EFMs can be calculated from the LDA measurement data using the specified assumptions. In the results section, the deviations of the flow rate resulting from the disturbed inflow conditions are described as a percentage error given by

$$\varepsilon = \frac{Q(\varphi) - Q_{ref}}{Q_{ref}} \cdot 100\ [\%]\,, \tag{5}$$

where $Q(\varphi)$ denote the modeled UFM and EFM flow rates. $Q_{ref}$ is the reference flow rate calculated with regard to fully developed measurements. $\varepsilon$ is expressed by a mean

and standard deviation with respect to the angular position $\varphi_j$ ($j \in [1, N_\varphi]$) of the beams and electrodes. In the calculation of $\varepsilon$, the correction factors in Eq. (6) and (8) are eliminated.

### 2.3.1 Ultrasonic flow meter

The flow rate $Q_{UFM}$ of a transit-time UFM with the transducers positioned at an angle of $\varphi_j$ (see Fig. 5) can be modeled using the equation given by

$$Q_{UFM}(\varphi_j) = k \cdot A \cdot w_p\,, \tag{6}$$

where $k$ is a $Re$-dependent correction factor and $A = \pi \cdot R^2$ the pipe's cross section. Moreover, $w_p$ is the averaged path velocity along the ultrasonic beams calculated from the difference of the transit times $t_{AB}$ and $t_{BA}$, which correspond to the signal times from transducers A to B and B to A, respectively.
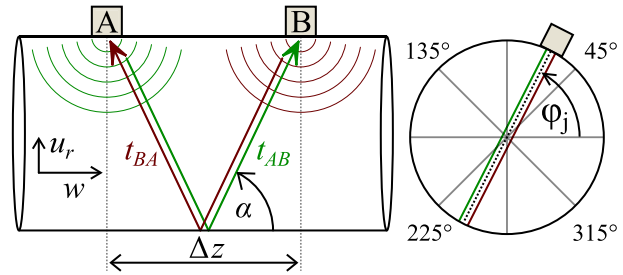
**Figure 5:** Illustration of a transit-time ultrasonic flow meter in reflection mode. The transducers A and B have an axial distance of $\Delta z$ and are located at $\varphi_j$ (here: 63°). $t_{AB}$ and $t_{BA}$ correspond to the ultrasonic transit times from A to B and B to A, whereas $u_r$ and $w$ denote the radial and axial velocity components.

For a derivation of $w_p$ in a direct path arrangement, see Moore et al. [18]. In a reflection alignment as illustrated in Fig. 5, the radial velocity component $u_r$ can be neglected (assuming $\mathrm{d}u_r/\mathrm{d}z = 0$ along the axial distance between the transducers $\Delta z$), as its influence on the propagation of the ultrasonic signal is compensated after the reflection on the wall. If it is further assumed that $\mathrm{d}w/\mathrm{d}z = 0$ along $\Delta z$, $w_p$ is independent from the inclination angle $\alpha$ and can be calculated representatively along a radial path with length $D$ given by

$$w_p = \frac{1}{D} \cdot \int_{-R}^{R} w\,\mathrm{d}r\,. \tag{7}$$

In Straka et al. [23], the same model calculated from LDA measurements was compared to clamp-on UFMs in

reflection mode ($\Delta z \approx 0.5 \cdot D$) exposed to the flow disturbance downstream of an SOP33. For the measurement distances greater than one diameter, the comparison resulted in deviations of $\approx 1\%$.

### 2.3.2 Electromagnetic flow meter

An EFM measures the voltage induced across the fluid through a magnetic field, which is proportional to the fluid's average velocity. For a circular cross section and the electrodes positioned perpendicular to the magnetic field at angles of $\varphi_j$ and $\varphi_j + 180°$, the flow rate $Q_{EFM}$ can be calculated according to

$$Q_{EFM}(\varphi_j) = k \cdot \iint_A w \cdot W(\varphi_j) \, dA \,. \tag{8}$$

Here, $k$ is a $Re$-dependent correction factor, whereas $W(\varphi_j)$ denotes the weight function as described by Shercliff [21] given by

$$W(\varphi_j) = \frac{R^4 - R^2 \cdot r^2 \cdot \cos(2 \cdot [\varphi_j - \varphi])}{R^4 - 2 \cdot R^2 \cdot r^2 \cdot \cos(2 \cdot [\varphi_j - \varphi]) + r^4} \tag{9}$$

and depicted in Fig. 6, which accounts for the different weighting of the flow field as a function of the distance to the electrodes. In proximity to the point electrodes, $W(\varphi_j)$ increases without bound and is therefore cut off at a maximum value of 2.5.

In contrast to UFMs, an EFM is generally not affected by non-axial velocity components, as only the flow perpendicular to the magnetic field contributes to the cre-
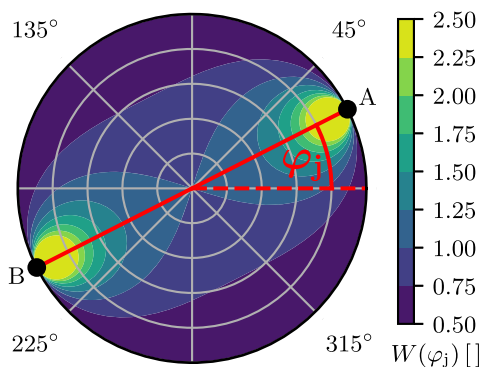


**Figure 6:** Contours of the Shercliff weight function [21] given by Eq. (9) used for the model of the electromagnetic flow meter. The point electrodes A an B are located at the pipe wall with angles of $\varphi_j$ and $\varphi_j + 180°$ (here: 27°, 207°) perpendicular to the magnetic field. $W(\varphi_j)$ is cut off at a maximum value of 2.5 in proximity to the electrodes.

ation of the potential difference. However, the model ignores the axial extent of the magnetic field and thus also assumes $dw/dz = 0$ along the sphere measurable for the electrodes. Other 2D and 3D based weight functions for circular and rectangular cross sections and different meter designs have been derived theoretically and numerically. An overview is given by Yin et al. [28].

# 3 Results and discussion

## 3.1 Description of the flow patterns

For the quantitative comparison of the LDA measurements downstream of the SOP33 and 90°-bend, contours of the secondary velocity component $u$ and the axial velocity component $w$ are presented in Fig. 7, 8 and 9. Its values are specified in multiples of the volumetric velocity $w_{vol}$, while the stream-wise distance between the disturbance and the measurement plane is expressed in multiples of the pipe diameter $D$.

### 3.1.1 Segmental orifice plate

As depicted in Fig. 8, the orifice geometry of the SOP33 located on the left results in a primary displacement of the core flow towards the opposite (right) side of the pipe. At a distance of $2.0 \, D$, the velocity values are highly accelerated and show a maximum of $1.9 \cdot w_{vol}$. At $Re = 5 \times 10^4$, the recirculation zone behind the orifice is still visible through the negative velocities, while the flow at the higher $Re$ has already reattached on the wall. Looking at the non-axial component $u$ in Fig. 7 (a), the dominant horizontal movement is directed towards the left, realizing the expansion of the flow over the entire pipe's cross section as the recirculation zone decreases.

Following a singular symmetric state measured at a distance of $5.1 \, D$, the secondary motion (now in accordance with the Dean vortex structure) results in a shift of the core flow to the left, similar to the observations made by Eichler [13] and Straka et al. [23] for the SOP7 and SOP33 in DN 80 and DN 200, respectively. After falling to a minimum at $15.2 \, D$, the velocity values of the asymmetric profiles increase again, and the radial distance of the peak velocity region gets smaller. Meanwhile, the values of the secondary component $u$ and accordingly the rotational velocity of the Dean vortices constantly decreases. Comparing the different $Re$ numbers, the (normalized) peak velocity values at $Re = 5 \times 10^5$ are smaller starting at $10.2 \, D$,
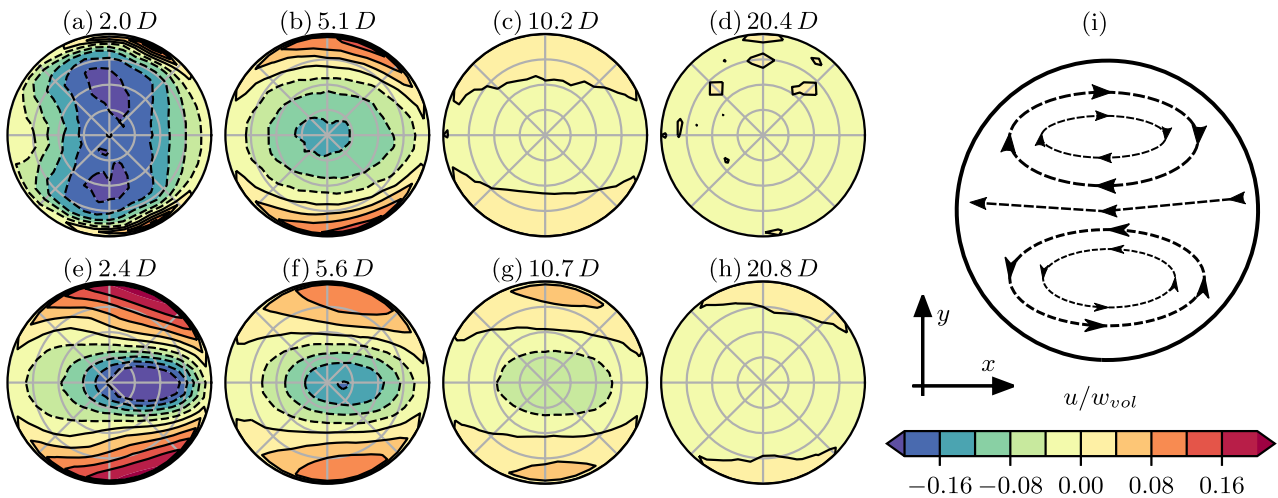
**Figure 7:** Contours of the non-axial velocity component $u$ in the horizontal direction of $x$, normalized with the volumetric velocity $w_{vol}$ for the segmental orifice plate with a segment area of $\approx 33\%$ at $Re = 5 \times 10^5$ (a–d) and the 90°-bend (e–h), presented at measurement positions between $\approx 2$ and 21 times the pipe diameter ($D$); (i) schematic illustration of the Dean vortex structure.
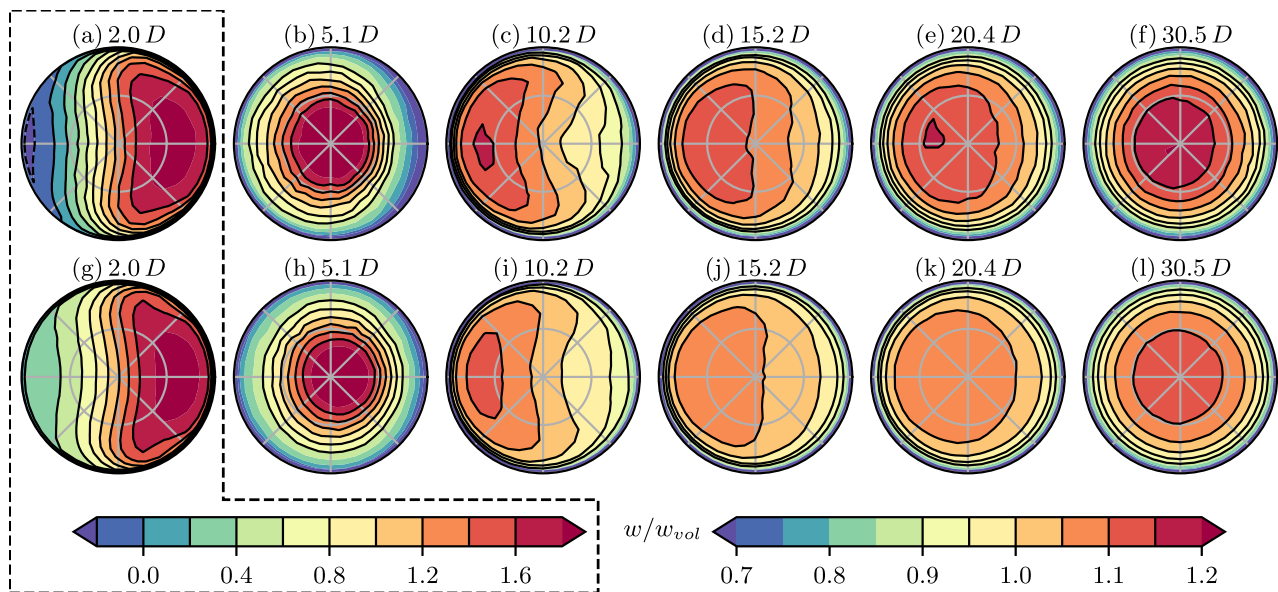


**Figure 8:** Contours of the axial velocity component $w$ normalized with the volumetric velocity $w_{vol}$ for the segmental orifice plate with a covered area of $\approx 33\%$. Measurements are presented at downstream positions between 2.0 and 30.5 times the pipe diameter ($D$), at Reynolds numbers of $Re = 5 \times 10^4$ (a–f) and $5 \times 10^5$ (g–l). Note that the profiles at 2.0 $D$ (a, g) use the color scale on the left.

which complies with the characteristics of a fully developed turbulent pipe flow.

### 3.1.2 90°-bend

In accordance with the flow phenomena inside the 90°-bend, the LDA velocity profiles measured at a distance of 2.4 $D$ (see Fig. 9 a/g) are highly asymmetric and have the shape of a crescent. The peak velocity regions are located at the outer left wall with maximum values of $1.3 \cdot w_{vol}$ and an area with low values of $0.8 \cdot w_{vol}$ is enclosed within the pipe center. At this position, the strength of the Dean vortices superimposing the flow have a maximum of $u = 0.25 \cdot w_{vol}$ (see Fig. 7 e).

Further downstream, the axial velocity values converge, resulting in a flat profile at 10.7 $D$ with velocities below 1.1 $\cdot w_{vol}$. As the disturbance relaxes towards the fully developed state, the velocities rise again, whereas the radial distance of the peak velocity and the values of $u$ con-
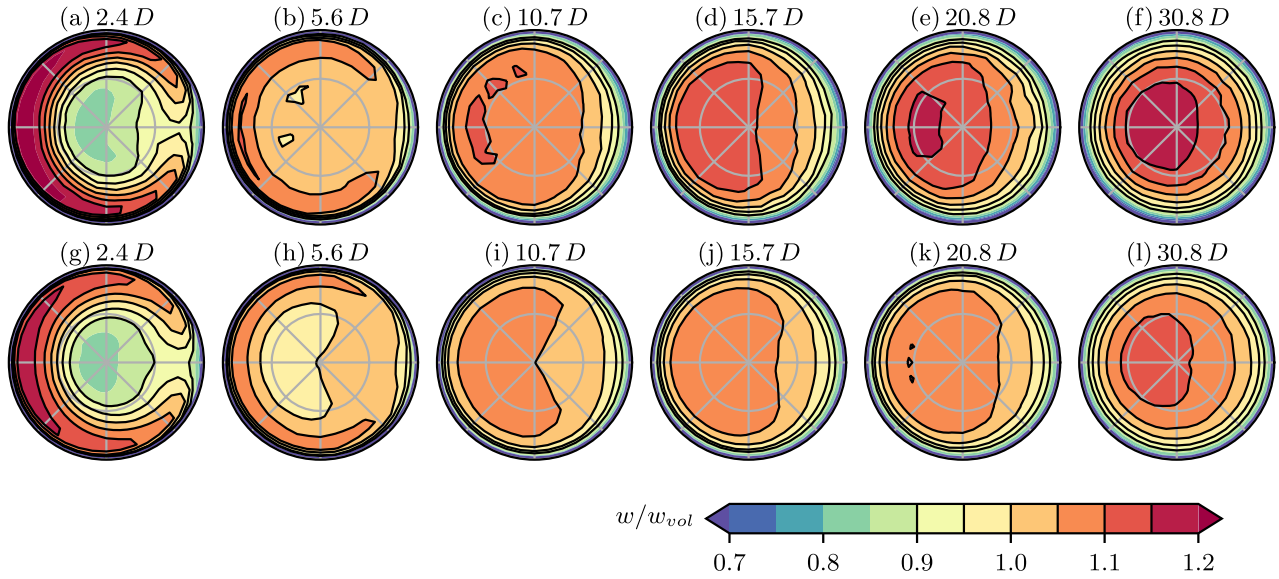
**Figure 9:** Contours of the axial velocity component $w$ normalized with the volumetric velocity $w_{vol}$ for the 90°-bend at $Re = 5 \times 10^4$ (a–f) and $5 \times 10^5$ (g–l), presented at measurement positions between 2.4 and 30.8 times the pipe diameter ($D$).

stantly decrease. Again, the (normalized) velocity values at the higher Reynolds number of $Re = 5 \times 10^5$ are smaller throughout all the measurement positions.

### 3.1.3 Qualitative comparison

With the orifice and outer curvature wall located at the left, both disturbances are oriented so that the Dean vortices downstream are equally aligned, rotating in accordance with the illustration in Fig. 7 (i). In the case of the 90°-bend, its magnitude ($\approx 0.25 \cdot w_{vol}$ at 2.4 $D$) correlates with the development of the crescent-shaped asymmetric profile, while the SOP initially causes a displacement to the right.

However, in between a distance of $\approx$ 5 and 10 $D$, the flow development downstream of the SOP33 shows similarities with the close-range effects downstream of the 90°-bend, as the core flow is heading left, displacing the slower flow on the orifice side. Since the rotational momentum of the secondary motion is far below the level of the 90°-bend ($\approx 0.12 \cdot w_{vol}$ at 5.1 $D$), the mechanism creates an asymmetry but is insufficient to develop the crescent-shaped profile. As the velocity values downstream of the 90°-bend converge, the profiles optically show a high degree of resemblance. This means, that the SOP33 reproduces the 90°-bend starting at $\approx$ 10 $D$, but does not reproduce the disturbance in the close-range distance.

In comparison to the SOP33, the degree of asymmetry downstream of the SOP7 observed by Eichler [13] is much weaker, especially with respect to the radial distance

of the core velocity region. No optical similarity with the 90°-bend can be determined in neither the near- nor the far-field range.

## 3.2 Analysis with performance indicators

In what follows, the experimental results are represented by performance indicators. This includes the mean profile factor $\langle K_P \rangle$, the mean asymmetry factor $\langle K_A \rangle$, the maximum turbulence factor $K_{Tu.\,max}$ and the maximum horizontal velocity $u_{max}$, calculated according to Equations (1), (2), (3) and (4). The development of the performance indicators within the measured distance range of $\approx$ 2 and 31 $D$ is depicted in Fig. 10. To allow a comparison with the SOP7, Fig. 10 includes the PIV measurements by Eichler [13], taken at measurement positions between 1 and 25 diameters at $Re = 4 \times 10^5$.

### 3.2.1 Mean profile factor

The similarities in the courses of the mean profile factor $\langle K_P \rangle$ (describing the peakness/flatness of the profile) illustrated in Fig. 10 (a) in between $\approx$ 10 and 31 $D$ quantitatively confirm the optical resemblance between the 90°-bend and the SOP33. Within that range, $\langle K_P \rangle$ rises from approximately 0.1 to 0.8, meaning that the profiles are comparatively flat in comparison to the fully developed reference conditions, where $\langle K_P \rangle$ = 1. In the case of the SOP33, the
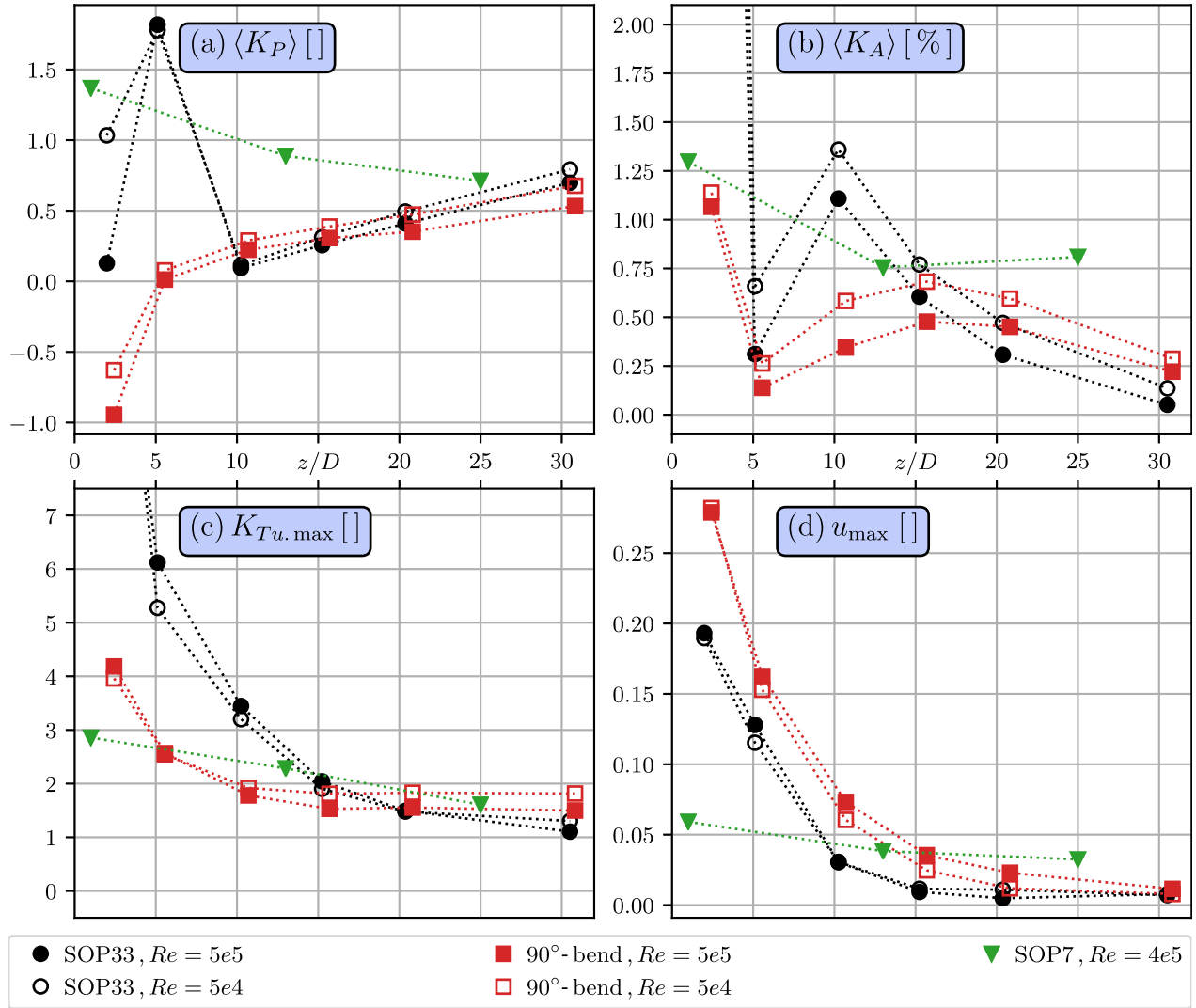
**Figure 10:** Performance indicators calculated from the LDA data downstream of the segmental orifice plate with a segment area of $\approx 33\%$ (SOP33) and the 90°-bend at Reynolds numbers ($Re$) of $5 \times 10^4$ and $5 \times 10^5$; (a): mean profile factor $\langle K_P \rangle$; (b): mean asymmetry factor $\langle K_A \rangle$; (c): maximum turbulence factor $K_{Tu.\,max}$; (d): maximum horizontal velocity $u_{max}$. Included are the PIV measurements by Eichler [13] of the standardized segmental orifice plate with a segment area of $\approx 7\%$ (SOP7) at a $Re$ number of $4 \times 10^5$. For a better orientation, the measurements are connected by dotted lines. For the SOP33 at a distance of 2.0 diameters, the values of $K_A$ (13.2 and 10.4 %) and $K_{Tu.\,max}$ (14.2 and 13.2) for $Re = 5 \times 10^4$ and $5 \times 10^5$ were cut off.

relaxation takes place at a noticeably faster rate, indicated through the slightly higher slope.

At a $2.4\,D$ distance to the 90°-bend, the negative values reaching a minimum of $\langle K_P \rangle \approx -0.9$ comply with the low values of the velocity in the pipe center and the concave shape of the profile. In contrast, the peak values up to $\langle K_P \rangle \approx 1.8$ in the case of the SOP33 at $5.1\,D$ correlate with the steep profiles and the high velocities in the pipe center. Despite the differences $2.0\,D$ downstream of the SOP33 (again due to the variation of the velocity in the center), the courses of $\langle K_P \rangle$ exhibit no clear $Re$-related effects.

As for the SOP7, the development of $\langle K_P \rangle$ is clearly different. While the missing peak observed for the SOP33

at the temporal symmetric state is simply not covered by the measurement positions, the values are much higher throughout the entire range, meaning that the profiles are much less flat or less disturbed.

### 3.2.2 Mean asymmetry factor

Starting with the 90°-bend, the mean asymmetry factor (describing the radial displacement of the velocity centroid) depicted in Fig. 10 (b) initially falls to an intermediate low of $\langle K_A \rangle \approx 0.2\%$ at $5.6\,D$, as the velocity values of the crescent-shaped profile converge. Further down-

stream, the peak values and thus, also $\langle K_A \rangle$, rises to a maximum of 0.5 % at 15.7 $D$ ($Re = 5 \times 10^5$) and subsequently falls towards the end, because the radial distance of the velocity peak decreases.

As for the SOP33, $\langle K_A \rangle$ has a very high value of 10.4 % at the strongly asymmetric profile at the 2.0 $D$ measurement position ($Re = 5 \times 10^5$) and reaches an intermediate low of 0.3 % at the (nearly symmetrical) state at a distance of 5.1 $D$. With the core velocity region shifted to the left, $\langle K_A \rangle$ increases to a maximum of 1.1 % at 10.2 $D$ and subsequently falls. In comparison to the 90°-bend, there is a similar progression starting at $\approx 15\,D$. Once again, the relaxation towards fully developed conditions emerges at a higher pace, expressed through the lower $\langle K_A \rangle$ at the last measurement position. For both the SOP33 and the 90°-bend, the lower $Re$ is connected to higher values of $\langle K_A \rangle$, presumably due to the constantly higher (normalized) velocity values.

The SOP7 creates comparatively high values of $\langle K_A \rangle$ throughout all measurement positions, exceeding the values of the 90°-bend and the SOP33 starting at $\approx 15\,D$. In the case of the SOP7, the displacement of the velocity centroid is connected to the large peak velocities. Furthermore, the development of $\langle K_A \rangle$ demonstrates the much slower abatement of the flow disturbance.

### 3.2.3 Maximum turbulence factor

A significant increase of the maximum turbulence factor $K_{Tu.\,max}$ (describing the extent of velocity fluctuations) illustrated in Fig. 10 (c) can be observed in proximity to all the disturbances, relaxing towards a nearly constant level at a distance of $\approx 15\,D$. A comparison between the SOPs reveals the correlation between the height of the orifice geometry and the turbulence intensity, connected to the production of turbulence kinetic energy in the recirculation zone. With a maximum value of 13.2 at 2.0 $D$ ($Re = 5 \times 10^5$), $K_{Tu.\,max}$ for the SOP33 exceeds the value of the SOP7 and the 90°-bend by a factor of 4.4 and 3.3. It can be concluded, that the higher values of $K_{Tu.\,max}$ also correlate with the faster transition of the flow disturbance towards reference conditions, expressed through the relaxation of $\langle K_P \rangle$ and $\langle K_A \rangle$.

### 3.2.4 Maximum horizontal velocity

As observed qualitatively, $u_{max}$ (describing the maximum non-axial velocity in the horizontal direction) depicted in Fig. 10 (d) has higher values in the case of the 90°-bend,

meaning that the rotation of the Dean vortices in the case of the SOP33 is comparatively lower. Throughout the measurement range, the values decrease in an exponential manner.

As for the SOP7, $u_{max}$ is smaller in proximity to the disturbance (by a factor of 3 in comparison to the SOP33), but abates at a much smaller rate, exceeding the SOP33 and the 90°-bend at distances of approximately $\approx 9$ and $16\,D$, respectively.

## 3.3 Modeled meter performance

To demonstrate the errors in the calculation of the flow rate, we model the performance of an ultrasonic flow meter in reflection mode and an electromagnetic flow meter according to Equations (6) and (8), which are exposed to the flow conditions downstream of the SOP33 and the 90°-bend. The percentage errors $\varepsilon_{\mathrm{UFM}}$ and $\varepsilon_{\mathrm{EFM}}$ are calculated according to Equations (5) and included in Fig. 11 as a function of the downstream distance, expressed by a mean and standard deviation with regard to the angular position of the ultrasonic beams and electrodes. Again, the PIV measurements of the SOP7 by Eichler [13] are included.

### 3.3.1 Ultrasonic flow meter

In the case of the 90°-bend, the error calculated for an ultrasonic flow meter $\varepsilon_{\mathrm{UFM}}$ (see Fig. 11 a) has a value of $-11.1\,(\pm 0.5)$ % at 2.4 $D$ ($Re = 5 \times 10^5$) and decays exponentially to a minimum of $-1.6\,(\pm 0.2)$ % at the measurement position at 30.8 $D$. Throughout the range, the mean error has a negative value and the angular dependency expressed by the standard deviation is below 0.7 %.

The negative sign can be linked to the consistently flattened and partially concave shape of the velocity profiles, quantified also by $\langle K_P \rangle$ in Fig. 10 (a). At fully developed reference conditions, the integral in Eq. (7) yields values for the averaged path velocity $w_p$ in the range of $w_p \approx 1.05 \cdot w_{vol}$, because the radial distance is not weighted in the line integral, resulting in an over-representation of the high velocities in the center region. Compensated by a $Re$-dependent correction factor $k$ in the range of $\approx 0.95$, $k \cdot w_p$ equals $w_{vol}$ and the correct flow rate can be calculated by multiplication with the pipe's cross section. When exposed to a comparatively flattened profile, $w_p$ takes on values closer to $w_{vol}$, resulting in $k \cdot w_p < w_{vol}$ and a negative deviation of the calculated flow rate with a maximum of $-5$ % for a theoretically uniform profile, where $w_p = w_{vol}$.
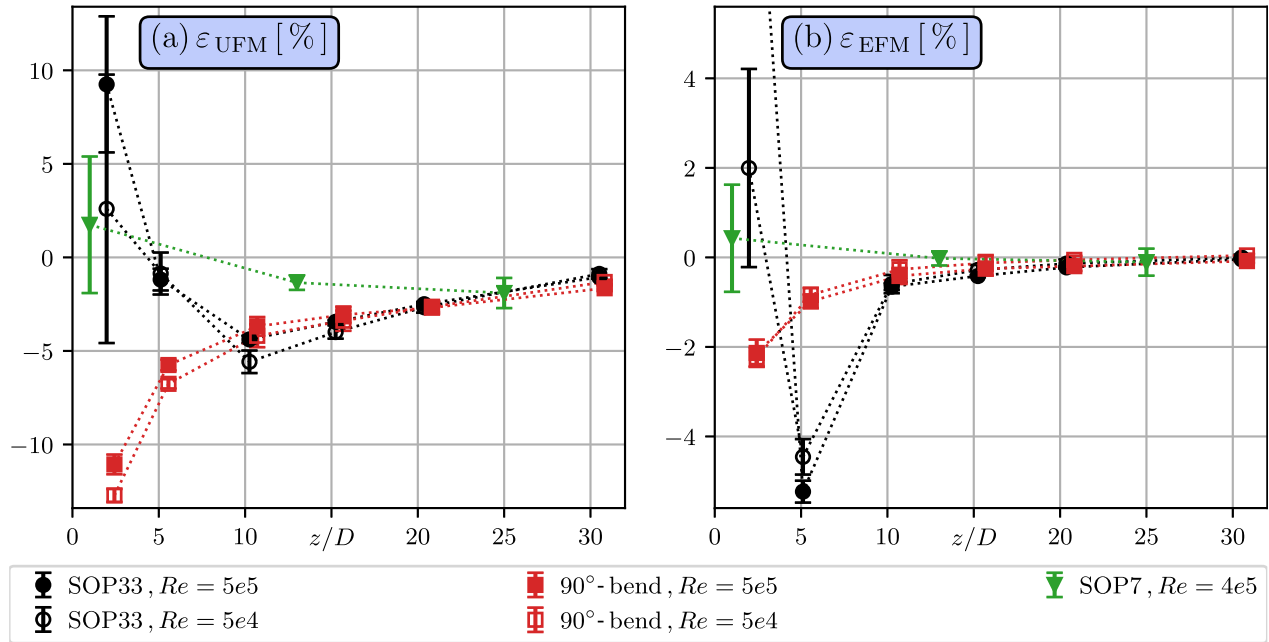
**Figure 11:** Meter error of an (a): ultrasonic flow meter (UFM) and (b): electromagnetic flow meter (EFM) expressed by a mean and standard deviation with regard to the angular position of the beams and electrodes, respectively, calculated from the LDA measurements downstream of the segmental orifice plate with a segment area of $\approx 33\%$ (SOP33) and the 90°-bend at Reynolds numbers of $5 \times 10^4$ and $5 \times 10^5$. Further included are the PIV measurements by Eichler [13] of a standardized segmental orifice plate with a segment area of $\approx 7\%$ (SOP7) at a $Re$ number of $4 \times 10^5$. For a better orientation, the measurements are connected by dotted lines. For the SOP33, $\varepsilon_{EFM} = 12.1\,(\pm 1.2)\,\%$ at $Re = 5 \times 10^5$ and a distance of 2.0 diameters was cut off.

In the case of a concave profile as observed up to a distances of $5.6\,D$ to the 90°-bend, $w_p$ takes on values smaller than $w_{vol}$ and the flow rate deviation falls below –5 %.

At 2.4 and $5.6\,D$, the crescent-shaped profiles in Fig. 9 (a/b, g/h) feature high and low velocities in the wall-near region opposing each other, which to some extent balance out in the path integrals calculated from $r = -R$ to $R$. For this reason, the standard deviations of 0.5 and 0.3 % ($Re = 5 \times 10^5$) are relatively low.

In comparison, the errors downstream of the SOP33 are initially positive, showing a maximum of 9.2 (±3.6) % ($Re = 5 \times 10^5$) and a higher standard deviation, especially at a distance of $2.0\,D$. Beginning at $\approx 10\,D$, the course of $\varepsilon_{UFM}$ is in line with the 90°-bend. This is different in case of the SOP7, which causes a much lower mean error ranging from 1.7 % to –1.9 % within the measurement range. Since the disturbance abates at a slower rate, $\varepsilon_{UFM}$ intersects with the courses of the 90°-bend and SOP33 at $\approx 25\,D$.

### 3.3.2 Electromagnetic flow meter

As depicted in Fig. 11 (b), the profiles downstream of the 90°-bend cause an exponentially decaying negative mean

error $\varepsilon_{EFM}$ and a low standard deviation for the model of the electromagnetic flow meter. In comparison to the UFM, the error is smaller, reaching a maximum deviation of –2.1 (±0.3) % at $2.4\,D$ ($Re = 5 \times 10^5$).

In contrast to the evident correlation between $\varepsilon_{UFM}$ and $\langle K_P \rangle$, the measurement deviation of the EFM is influenced by a variety of effects related to asymmetry ($\langle K_A \rangle$), shape ($\langle K_P \rangle$) and the peak velocity. In the presence of an asymmetry, the velocities in proximity to one or both electrodes may be increased, increasing the value of the surface integral in this strongly weighed area, whereas secondly, the velocities in the greater part of the cross section are reduced, partially reducing the surface integral.

In case of the 90°-bend and the SOP33 starting at $10.2\,D$, the second effect is predominant, resulting in a negative error. In the case of the SOP33 at $2.0\,D$, the first effect outweighs the second for most angular positions, because the peak velocities are very high. Here, the mean error is positive, reaching a maximum of 12.1 (±1.2) % at $Re = 5 \times 10^5$. As for the (nearly symmetrical) pointed profile at $5.1\,D$, the velocity values in proximity to both electrodes are comparatively low, resulting in a negative error with a value of –5.2 (±0.2) %.

Following the fluctuations at 2.0 and $5.1\,D$, the error curve of the SOP33 is similar to the 90°-bend starting at

$\approx 10\,D$. In comparison, the SOP7 causes a maximum error of only $0.4\,(\pm 1.2)\,\%$ at $1.0\,D$, falling towards $-0.0\,(\pm 0.1)\,\%$ and $-0.1\,(\pm 0.3)\,\%$ at 13 and $25\,D$, respectively.

# 4 Conclusions

This study examined SOPs and their ability to reproduce the flow disturbance created by a 90°-bend. On the basis of LDA measurements of an SOP33, a 90°-bend and recent investigations of an SOP7, we demonstrated the downstream flow development by means of a qualitative description of the flow patterns and a quantification with a set of performance indicators. Furthermore, the varying influence of the disturbed flow conditions was illustrated through the performance of an ultrasonic and electromagnetic flow meter.

Both meters were emulated with a model representing the flow measurement principles in a basic form. Accordingly, the study did not reflect on the bandwidth of model variations and accuracy classes available on the market. In the upper price range, EFMs are usually equipped with some type of internal flow conditioning, for example a reduced rectangular cross section geometry to homogenize the inlet flow profile. A single-beam alignment (in direct path or reflection mode) is widely used for ultrasonic heat and water meters in households and common for clamp-on devices, whereas most in-line sensors for industrial applications use multi-beam alignments and chord paths with proprietary weighting. Elaborate meter designs are generally superior to the applied models regarding the susceptibility towards the inflow conditions and may show a smaller absolute measuring error for any disturbance. Nevertheless, it can be expected that there are similar relative differences resulting from the unequal flow conditions created by the 90°-bend and the orifices. Consequently, an assessment of the disturbance generators with respect to their ability to verify the compliance with the maximum permissible error limits at the presence of a 90°-bend is transferable to advanced meter designs and their respective accuracy classes.

The results showed, that the SOP7 provides an insufficient degree of asymmetry and secondary components in comparison to the 90°-bend. Major differences could be determined in terms of the qualitative flow development and by means of performance indicators. Both the error curves of the UFM and EFM showed, that the absolute meter error caused by the SOP7 is below the 90°-bend by at least a factor of 2 within a range up to 15 diameters. Using a single disturbance generator to cover the superordinate category of asymmetric flow disturbances in a standardized test is justified due to the expenditure of time. But while a representation of pipe joints and gate valves seem plausible given the geometrical similarities, the SOP7 does not serve as a substitute for the 90°-bend.

A better similarity could be determined downstream of the SOP33 within a distance range of approximately 10 to 20 diameters. This makes it a reliable test object in preparation for a flow meter installed in a similar distance to a 90°-bend. However, the characteristic crescent-shaped profiles in close proximity to the 90°-bend could also not be reproduced. In the flow disturbance test according to the standards for water meters [4, 3], the distance to a meter under test is specified by profile sensitivity classes provided by the manufacturer, ranging from 0 to 15 pipe diameters. A meter calibrated at a distance of, for example, five diameters to the set of disturbance generators is attested to be installed at an equal distance behind a 90°-bend and other components. Given the different flow development up to a distance of 10 diameters, the SOP33 does not represent a suitable alternative for the SOP7.

In the interest of consumer protection and prevention of market distortions, further studies are necessary to develop a disturbance generator that creates the profile of a 90°-bend in the entire calibration range. Building on the results of this study, a revised orifice design must deal with the insufficient intensity of the Dean vortices following the shift of the velocity core region or prevent the shift by changing the direction of rotation.

# References

1. VDI/VDE 2640 Blatt 1. Measurement of fluid flow in closed conduits; general guidelines and mathematical basics. Standard, 1983.
2. ISO 5167-1. Measurement of fluid flow by means of pressure differential devices inserted in circular cross-section conduits running full – Part 1: General principles and requirements. Standard, 2003.
3. OIML R 49-2. Water meters for cold potable water and hot water – Part 2: Test methods. Standard, 2013.
4. ISO 4064-2. Water meters for cold potable water and hot water – Part 2: Test methods. Standard, 2014.
5. EN 1434-4. Heat meters – Part 4: Pattern approval tests. Standard, 2016.
6. EN 10253-2. Butt-welding pipe fittings – Part 2: Non alloy and ferritic alloy steels with specific inspection requirements. Standard, 2017.

7.  EN 10253-4. Butt-welding pipe fittings – Part 4: Wrought austenitic and austenitic-ferritic (duplex) stainless steels with specific inspection requirements. Standard, 2017.

8.  H. Akima. A new method of interpolation and smooth curve fitting based on local procedures. *J. ACM*, 17(4):589–602, 1970. http://doi.org/10.1145/321607.321609.

9.  N. Crawford, S. Spence, A. Simpson, and G. Cunningham. A numerical investigation of the flow structures and losses for turbulent flow in 90 degrees elbow bends. *Proc. Inst. Mech. Eng, Part E: J. Process Mech. Eng.*, 223(1):27–44, 2009.

10. W. R. Dean. Note on the motion of fluid in a curved pipe. *Phil. Mag*, 20:208–223, 1927. http://doi.org/10.1080/14786440708564324.

11. F. Durst, M. Fischer, J. Jovanovic, and H. Kikura. Methods to set up and investigate low reynolds number, fully developed turbulent plane channel flows. *J. Fluids Eng.*, 120(3):496–503, 1998. http://doi.org/10.1115/1.2820690.

12. P. Dutta, S. K. Saha, N. Nandi, and N. Pal. Numerical study on flow separation in 90° pipe bend under high reynolds number by k-$\epsilon$ modelling. *Engineering Science and Technology, an International Journal*, 19(2):904–910, 2016. http://doi.org/10.1016/j.jestch.2015.12.005.

13. T. Eichler. *Vergleich der „Stereo Particle Image Velocimetry" (SPIV) mit rückgeführten Messverfahren und Untersuchung definiert gestörter Strömungszustände in geschlossenen Rohrleitungen*. PhD thesis, Technische Universität Berlin, 2013.

14. K. Gersten and H. Herwig. *Strömungsmechanik. Grundlagen der Impuls-, Wärme- und Stoffübertragung aus asymptotischer Sicht*. Vieweg-Verlag, Braunschweig/Wiesbaden, 1 edition, 1992.

15. A. Kalpakli. Experimental study of turbulent flows through pipe bends (licentiate dissertation). Technical report, Royal Institute of Technology, KTH Mechanics, Stockholm, Sweden., 2012. URL: http://www.mech.kth.se/thesis/2012/lic/lic_2012_athanasia_kalpakli.pdf.

16. G. Mattingly and T. Yeh. Effects of pipe elbows and tube bundles on selected types of flowmeters. *Flow Meas. and Instrum.*, 2(1):4–13, 1991.

17. W. Merzkirch, editor. *Fluid Mechanics of Flow Metering*. Springer-Verlag, 2005. http://doi.org/10.1007/b138000.

18. P. I. Moore, G. J. Brown, and B. P. Stimpson. Ultrasonic transit-time flowmeters modelled with theoretical velocity profiles: Methodology. *Meas. Sci. Technol.*, 11:1802–1811, 2000.

19. U. Müller. Guidelines for the fluid mechanical validation of calibration test-benches in the framework of EN 1434, 2009.

20. Durchflussmessanlage für Kaltwasser (20 °C bis 40 °C) im Volumenstrombereich von $10\,\mathrm{m^3\,h^{-1}}$ bis $180\,\mathrm{m^3\,h^{-1}}$. Qualitätsmanagement-Arbeitsanweisung, Physikalisch-Technische Bundesanstalt, 2018.

21. J. A. Shercliff. Relation between the velocity profile and the sensitivity of electromagnetic flowmeters. *Appl. Phys.*, 25:817–818, 1954. http://doi.org/10.1063/1.1721749.

22. M. Straka, T. Eichler, C. Koglin, and J. Rose. Similarity of the asymmetric swirl generator and a double bend in the near-field range. *Flow Meas. and Instrum.*, 70:101647, 2019. https://doi.org/10.1016/j.flowmeasinst.2019.101647.

23. M. Straka, A. Fiebach, C. Koglin, and T. Eichler. Hybrid simulation of a segmental orifice plate. *Flow Meas. and Instrum.*, 60:124–133, 2018. http://doi.org/10.1016/j.flowmeasinst.2018.02.006.

24. K. Sudo, M. Sumida, and H. Hibara. Experimental investigation on turbulent flow in a circular-sectioned 90-degree bend. *Exp. Fluids*, 25(1):42–49, 1998. https://doi.org/10.1007/s003480050206.

25. J. Thorns. Analytische und experimentelle Untersuchung der Messunsicherheit eines Geschwindigkeitsnormals zur Kalibrierung von LDV-Systemen, 2010. Diplomarbeit, Technische Universität Berlin.

26. Z. Wang, R. Örlü, P. Schlatter, and Y. M. Chung. Direct numerical simulation of a turbulent 90° bend pipe flow. *Int. J. Heat Fluid Fl.*, 73:199–208, 2018.

27. A. Weissenbrunner, A. Fiebach, S. Schmelter, M. Bär, P. Thamsen, and T. Lederer. Simulation-based determination of systematic errors of flow meters due to uncertain inflow conditions. *Flow Meas. and Instrum.*, 52:25–39, 2016.

28. S. Yin, B. Li, K. Meng, and J. Chen. Performance differences of an electromagnetic flow sensor with nonideal electrodes based on different-dimensional weight functions. *IEEE T. Instrum. Meas.*, 67(7):1738–1748, 2018.

# Bionotes

**Dipl.-Ing. (FH) Martin Straka**
Physikalisch-Technische Bundesanstalt, Abbestr. 2–12, 10587 Berlin, Germany
**martin.straka@ptb.de**

Research associate at the Working Group „Flow Analysis for Thermal Energy Measurement" at the Physikalisch-Technische Bundesanstalt, Institute Berlin. His field of work includes the characterization of pipe flow conditions with numerical and laser-optical methods.

**Dipl.-Ing. Christian Koglin**
Physikalisch-Technische Bundesanstalt, Abbestr. 2–12, 10587 Berlin, Germany
**christian.koglin@ptb.de**

Engineer at the Working Group „Flow Analysis for Thermal Energy Measurement" at the Physikalisch-Technische Bundesanstalt, Institute Berlin. His range of tasks involves the supervision of test rigs and laser-optical measurement systems.

**Dr. Thomas Eichler**
Physikalisch-Technische Bundesanstalt,
Abbestr. 2–12, 10587 Berlin, Germany
**thomas.eichler@ptb.de**

Head of the Working Group „Flow Analysis for Thermal Energy Measurement" at the Physikalisch-Technische Bundesanstalt, Institute Berlin.